Journal of Medical Systems (2019) 43: 225
https://doi.org/10.1007/s10916-019-1315-4

IMAGE & SIGNAL PROCESSING

An Efficient Melanoma Diagnosis Approach Using Integrated HMF Multi-Atlas Map Based Segmentation

D. Roja Ramani[1] · S. Siva Ranjani[2]

Received: 10 March 2019 / Accepted: 25 April 2019 / Published online: 12 June 2019

Abstract
Melanoma is a life threading disease when it grows outside the corium layer of the skin. Mortality rates of the Melanoma cases are maximum among the skin cancer patients. The cost required for the treatment of advanced melanoma cases is very high and the survival rate is low. Numerous computerized dermoscopy systems are developed based on the combination of shape, texture and color features to facilitate early diagnosis of melanoma. The availability and cost of the dermoscopic imaging system is still an issue. To mitigate this issue, this paper presented an integrated segmentation and Third Dimensional (3D) feature extraction approach for the accurate diagnosis of melanoma. A multi-atlas method is applied for the image segmentation. The patch-based label fusion model is expressed in a Bayesian framework to improve the segmentation accuracy. A depth map is obtained from the Two-dimensional (2D) dermoscopic image for reconstructing the 3D skin lesion represented as structure tensors. The 3D shape features including the relative depth features are obtained. Streaks are the significant morphological terms of the melanoma in the radial growth phase. The proposed method yields maximum segmentation accuracy, sensibility, specificity and minimum cost function than the existing segmentation technique and classifier.

Keywords Depth features · Lesion color texture (LCT)–Streax (STR) · Multi-atlas map · Melanoma diagnosis · Patch-based label fusion

Introduction

Skin Cancer can be classified as melanoma and non-melanoma type. Per annum, around 2-3 million people are affected by non-melanoma and 1,32,000 people are affected by melanoma across the globe [1]. In United States, the death rate of 75% is due to the melanoma cancer [2, 3]. This rate is very high when compared to non-melanoma type. In the previous decades, 2.6% increase in the death rate is observed per annum is observed in melanoma case. About 95% of survival rate is achieved if the melanoma is detected in early stages. Early detection also reduces the cost of treatment. But this early detection is highly a challenging one. Only 13% of survival rate is possible in case of advanced melanoma and the cost of the advanced melanoma treatment is also too high [4].

Skin lesions are diagnosed by Epiluminescence Microscopy (ELM) [5].Non-invasive dermoscopy is adopted by dermatologist experts. Gel is applied on the skin lesions to perform dermoscopy. Magnified skin images are obtained by digital imaging systems like stereomicroscope or dermatoscope. Additional color structures and pattern data can be obtained by using this magnified skin lesion images. These data's can be obtained by naked eye. Diagnosis and type of skin lesions can be identified by the use of this additional information [6]. Diagnosis of skin lesions can be done using Menzies approach [1], 7-point checklist [2], Border, Color and Diameter (ABCD) [3], Asymmetry and ABCD and Evolution (ABCDE) [4]. Dermoscopy and classical algorithms are used to improve the diagnosis rate of about 5-30%. This improvement is far better than the manual examination [7]. Melanoma and non-melanoma skin lesions makes the

This article is part of the Topical Collection on *Image & Signal Processing*

✉ D. Roja Ramani
rojaramanid@sethu.ac.in; rosevsroja@gmail.com

S. Siva Ranjani
ssivaranjani@sethu.ac.in; sivaranjani222@gmail.com

[1] Department of Information Technology, Sethu Institute of Technology, Virudhunagar, India

[2] Department of Computer Science and Engineering, Sethu Institute of Technology, Virudhunagar, India

process of diagnosis as a complex and difficult one. Skill level of dermatologists also has an impact on diagnosis accuracy.

The usage of Computer-Aided Diagnosis (CAD) can efficiently handle this issue. Advanced image processing techniques and decision making mechanisms are available for building CAD system [5] to facilitate early diagnosis of melanoma. Using shape, color and texture features, various dermoscopy systems have been developed. The developed sytems also includes the decision support mechanisms [7–18]. Dermoscopy techniques based on surface illumination are easily available. Illumination based techniques are also inexpensive. Accurate diagnosis depends on the estimation of skin lesion depths. Techniques like Three-Dimensional high-frequency ultrasound images [6], Nevoscopy [19], acoustic microscopy [20] and high-frequency ultrasound [21] are used for estimating the skin lesion depth. These techniques are also used for the construction of 3 D volumes. Dermoscopic imaging systems are costly and their availability is a matter of concern.

The segmentation and extraction of 3D depth features, Lesion Color Texture (LCT)–Streax (STR) features to accurately diagnose the melanoma in the skin image by an integrated approach is presented in this paper. The accuracy can be improved by combing the label information as non-rigid registration framework. The intensity values play a major role in classifying different types of tissues rather than the discrete labels. Encoding of skin regions spatial consistency for multi-region segmentation is done by applying a Partially-Ordered Potts (POP) model. In PoP model, multi-region segmentation can be done by introducing region order. Depth map obtained from 2D dermoscopic image is used to reconstruct the structure tensor of 3D lesion.

The 3D lesion is constructed by attaching the data related to depth map with 2D surface. Relative depth features and shape feature can be extracted by using this 3D reconstructed skin lesion data. Radial growth phase of malignant melanoma is depends on the streaks [22, 23]. Streak lines are analyzed by its position and spatial arrangement. Skin lesion is again classified as regular, irregular and absent streaks. The capability of Deep Convolutional Neural Networks (CNN) are used in various fine-grained object categories. A trained CNN is used classify the skin lesions. The details used by the CNN are disease labels and pixels. The performance analysis result shows that the proposed method yields maximum segmentation, sensibility, specificity and minimum cost function than the existing segmentation technique and classifier.

Automatic recognition of the streaks aids in building the computer-aided system for melanoma detection. Streaks are vital morphological terms of the melanoma in the radial growth phase [7, 24]. Streaks are the local dermoscopic features of the lesions and appear symmetrically over the entire skin lesion. Irregular streaks are the critical features that show highest association with melanoma. The positioning and spatial arrangements of the streak lines are analyzed. The skin lesion is further classified as a lesion with the absent, regular and irregular streaks [8].Multi-Atlas Segmentation (MAS) is used to yield better segmentation accuracy than the single-atlas [9–12]. In this approach, each atlas is available and potentially used for segmenting the image. A pairwise registration is applied between the new image and each atlas image. The registration results are used to propagate the atlas labels to the image coordinates. The most frequent label is selected at each voxel. It utilizes a group of atlases that denote the inter-subject variability of the skin region. The target image to be segmented is registered to each atlas and the propagated labels from multiple atlases are combined together to form a compact segmentation. In MAS, the atlas images are warped to the target image by the registration, and corresponding warped atlas labels are combined to produce an estimated segmentation of the target image. The advantages of the multi-atlas segmentation are described as

- It accounts for the anatomical shape inconsistency by using multiple atlases.
- It is highly robust due to the minimum segmentation errors associated with single atlas propagation when combining multiple atlases.
- The compact segmentation is less likely to be affected, when an individual atlas does not match the target image well or when serious registration errors occur for an individual atlas.

The main contributions of the proposed work are

- The 3D image reconstruction is achieved by fitting the depth map assessed to the underlying 2D surface.
- The low contrast and fuzzy streak lines are detected and the detected segments are used for extracting the clinically inspired feature sets for the orientation analysis of the structure.
- The HMF model indirectly encodes the definite region order or layout by the additional flows. This avoids confronting the challenging region order constraint clearly.
- The HMF regularizes each hierarchy level independently, while allowing accounting for the variations in smoothness of different objects, with minimum computational burden to a Potts model approach.
- The patch-based label fusion model is expressed in a Bayesian framework to improve the segmentation accuracy.
- Missing information in the lesion is computed by the LCT.
- By incorporating the label information into a non-rigid registration framework, the segmentation accuracy is improved.

The sections of the manuscript are drafted in the following order: Section II describes an overview of the existing techniques for segmenting, extracting important features and classifying the skin lesion images to accurately diagnose the melanoma. Section III explains the proposed work including parallelized Hierarchical Continuous Max-Flow (HMF) Model, Patch-based label fusion model, Feature extraction and classification. Section IV discusses about the comparative result analysis of various segmentation techniques. Section V concludes the work.

Related works

Skin lesion in the dermoscopic images are identified by Segmentation techniques. Abuzaghleh et al. [13] formulated a non-invasive automated system to analyze the skin lesion images for the early detection and prevention of melanoma. A real-time alert helps to prevent the skin burns caused by the sunlight. Efficient classification of the benign, different, and melanoma images with high accuracy is achieved. Glaister et al. [14] used texture features to segment the skin lesion. High accuracy of segmentation was achieved by this method. Jafari et al. [15] Used deep CNN to extract the lesion region.. Segmentation mask is created by generating label for each pixel and combining the local and global contextual information. Some post-processing operations are applied for the further refinement of the mask. High segmentation accuracy is achieved when compared with the existing algorithms.

Peruch et al. [16] segmented the melanocytic lesion by a new technique called Mimicking Expert Dermatologist Segmentation (MEDS). The segmentation combines a thresholding scheme that reproduces the intellectual process of the dermatologists with numerous independent optimizations. MEDS is extremely quick for the segmentation of medium-resolution images by using minimum computational resources. Features like shape, color and texture based automatic classification quantification techniques produces best results when compared to the manual diagnostic performance. Ma and Tavares [17] presented a complete review of the preprocessing and post-processing operations of the skin lesion images, with a specific emphasis on the quantification and classification of the pigmented skin lesions. Navarro et al. [18] proposed a combined image segmentation and registration algorithm for the accurate extraction of features to assess the evolution of the lesion. The lesion-size feature enabled development of the automatic diagnosis systems to easily evaluate the growth of skin lesion.

Kasmi et al. [25] applied a biologically inspired Geodesic Active Contour (GAC) technique for the segmentation of skin lesion. Automatic contour initialization is employed at the proximity to the boundary of actual lesion. The border is smoothed to impersonate the natural skin lesions. The GAC approach yielded accurate segmentation of skin lesion with minimum XOR error. Pennisi et al. [26] segmented the skin lesions of dermoscopic images by an automated algorithm. The presented algorithm is quick and produces high accuracy even though the image contains the oil bubbles, reflections and other flaws. Mittal et al. [27] identified the skin lesions using an innovative approach. The quality of skin lesion images are improved by Median filtering and Sobel edge detection approaches. The efficiency of the proposed segmentation approach is measured by calculating the entropy of images with different skin disease. Patel et al. [28] presented a method for segmenting the skin lesions using the clustering technique. The final clustered output is compared with the reference image to detect the different types of lesion. Kaur and Joshi [22] diagnosed the melanoma in the dermoscopic image by identifying the presence of pigment networks using various classification and feature extraction methods. Esteva et al. [23] applied end-to-end trained Deep CNN to classify the skin lesions. The proposed approach enabled efficient classification of the most common and deadliest skin cancers. Ma and Tavares [29] used a deformable model to segment dermoscopic images to find skin lesions. He differentiated the normal skin and skin lesion by the color information in the image. The speed function and the stopping criterion of the deformable model is defined by the combination of variations in the color channels of the image.

Bi et al. [30] combined the Image-wise Supervised Learning (ISL) and Multi-scale Super pixel based Cellular Automata (MSCA) to segment the skin lesion. High accuracy can be produced by using the proposed method. Al-abayechi et al. [31] formulated a novel technique for the segmentation of melanoma in the images. The watershed algorithm is applied for segmentation with morphological operation for the accurate segmentation of the skin lesion area. The proposed technique yielded maximum segmentation accuracy up to 96.47%. Ross-Howe and Tizhoosh [32]improved the performance of U-Net architecture by using pre and post processing techniques. Local binary patterns and wavelet decomposition are used to enhance the raw grayscale images used as input features of the network architecture.

Li and Shen [33] proposed a framework comprising multi-scale fully-convolutional residual networks and a Lesion Index Calculation Unit (LICU) for efficient lesion segmentation and classification. LICU is used to calculate the importance of a pixel for the classification of lesion. The proposed Lesion Feature Network (LFN) yields best average precision and sensitivity. Codella et al. [34] described the design and implementation of algorithms for the automated diagnosis of the melanoma. The proposed task is divided into lesion segmentation, feature detection, and disease classification. Highest performance is achieved using the ensembles of the deep learning approaches.

Jadhav et al. [35] presented the challenge of automatic detection of melanoma lesion on the skin images based on the concept of deep learning. Deep learning using the CNN architecture is able to efficiently detect the melanoma lesion. Nida et al. [36] proposed a deep learning RCNN for the automated segmentation of melanoma region using dermoscopic images. It precisely detects the multiple affected regions in the form of bounding boxes that simplify localization through Fuzzy C-Means (FCM) clustering.

Nasir et al. [37] developed a method for the classification of melanoma and benign skin lesions using uniform segmentation and feature selection based approach. A novel Boltzman Entropy method is implemented for selecting the fused features. The proposed approach yields better sensitivity, specificity, accuracy and F-score than the existing methods. Ebenezer and Rajapakse [38] applied a fully automated method for the accurate segmentation of the lesion boundaries from the dermoscopic images. A U-net deep learning network is trained on the publicly available data. The use of intensity, color, and texture enhancement operations are introduced as pre-processing steps and morphological operations and contour identification are used as post-processing steps.

Existing segmentation techniques suffer from low accuracy and high cost due to the presence of artifacts and significant illumination variations. The accurate recognition of melanoma is particularly challenging due to the low contrast between the lesions and skin, visual similarity between the melanoma and non-melanoma lesions, etc. There is a need to optimize the performance and investigate the correlation between the skin burn and neural activity in the brain. The texture-based skin lesion segmentation is to be tested additionally on a wide range of images. The melanoma cases are incorrectly classified using the locally-processed mobile applications. This work proposes an integrated segmentation and Third Dimensional (3D) feature extraction approach for the accurate diagnosis of melanoma. The proposed method yields maximum segmentation accuracy, sensibility, specificity and minimum cost function than the existing segmentation technique and classifier.

I. Proposed work

Initially, the image dataset is applied to the segmentation process. The parallelized HMF segmentation and multi-atlas map segmentation based on the Patch-based label fusion are used to segment the skin lesion image. The label information is combined into a non-rigid registration framework to increase accuracy, as the discrete labels can be less indefinite than the intensity values in distinguishing different types of tissues. A POP model is applied for the multi-region segmentation for encoding the spatial consistency of the skin regions. A custom label/region order constraint is introduced to the PoP model to the multi-region segmentation. A multi-atlas method is employed for the image segmentation. The 3D depth features, Lesion Color Texture (LCT)–Streax (STR) features are extracted from the image. The 3D lesion represented as structure tensors is reconstructed using a depth map obtained from the 2D image. Deep CNN is applied for the classification of the images by dividing disease into fine-grained training classes based on the fine-grained information lying within the taxonomy structure. During inference, the CNN outputs a probability distribution over these fine-grained training classes. The probabilities of their descendants is summed up together to regain the probabilities for coarser-level classes of interest. Figure 1 illustrates the flow diagram of the proposed work. Table 1 shows the symbols and descriptions.

A. *Parallelized Hierarchical Continuous Max-Flow (HMF) Model*

The U-shaped relaxed partially-ordered Potts model is solved by introducing a continuous approach called max-flow approach. A flow maximization model is implemented. It is a spatially continuous model and it is equivalent to Potts model. Continuous max flow approach is used to specify two-level hierarchical flow configuration in initial conditions.

- Terminal ‘s’ is added as source of the flows and ‘t’ is added as the sink of the flows. At upper level, replica images Ω_C and Ω_B are in parallel. The replica images are with respect to $\mathcal{R}_C$ and $\mathcal{R}_B$. At lowest level, three replicas $\Omega_{s,\,m,\,b}$ images are in parallel. This is with respect to $\mathcal{R}_{s,m,b}$
- Position ‘x’ of Ω_C and Ω_B are linked with the source‘s’. Free source flow $p_o(x)$ is defined. At each$\Omega_{s,\,m,\,b}$, $x \in \Omega_C$ is linked to the same pixel ‘x’. Free flow $p_C(x)$ is defined.

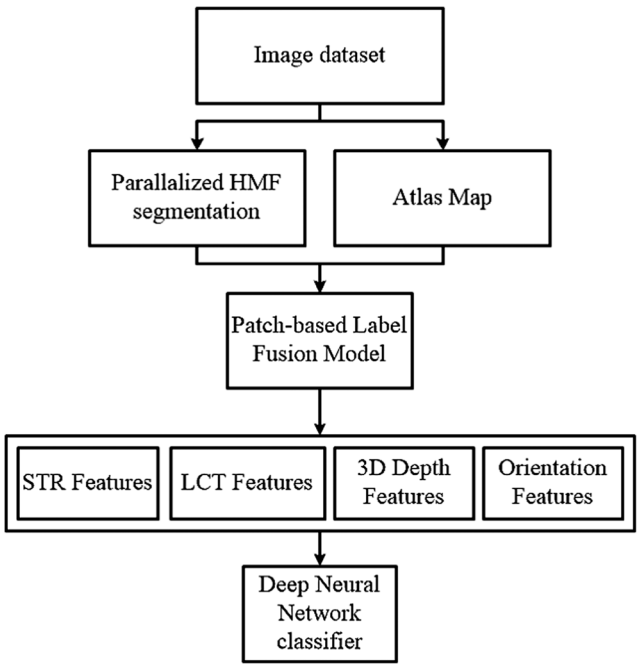

Fig. 1 Flow diagram of the proposed work

Table 1 Symbols and Descriptions

Symbols	Descriptions
s	Source Terminal
t	Sink terminal
$\mathcal{R}_C$	Skin region
$\mathcal{R}_B$	Background region
$\mathcal{R}_s$, $\mathcal{R}_m$ and $\mathcal{R}_b$	Sub-regions of skin
Ω_C and Ω_B	Image replicas
$\Omega_{s,\,m,\,b}$	Replicas of sub-regions
x	Pixel, Voxel
$p_o(x)$	Free source flow
$p_C(x)$	Free blood flow
$p_i(x)$	Sink flow
$q_i(x)$	Spatial flow
L1, L2	Label sets
'C'	Skin region
'B'	Background
Ω_i	Bottom-level image domain
$u_i(x)$	Labeling functions
T	Step-size for the convergence
$G_i^k(x)$	Flow residue function
I	Target image
I_n	Atlas image
$I_n^{'}(x)$	Deformed Atlas image
$L_n^{'}(x)$	Deformed Label map
Δx	Registration error between the target and deformed images
M	Random vector field
N	Number of atlases
K	Number of candidate voxels in a local neighborhood
Ω	3D lattice
$M(x)$	Mapping for the voxel
L	Label map
$\hat{L}$	Estimate of the label map
P	Joint probability for observing the target image and label map
Δ_{M_2}	Shift between the center voxel 'x' and M_2^{th} candidate voxel
$I(x)$	Intensity levels at the target voxels
$I_{M_1}^{'}$	Intensity levels at the respective voxels
σ_1	Standard deviation of the Gaussian distribution
$S(x)$	Patch centered at the voxel 'x'
$\lvert S(x)\rvert$	Number of voxels in the patch
$\lvert\Delta_{M_2}\rvert$	Magnitude of the shift vector Δ_{M_2} between the target and atlas patches
$\delta_{i,\,j}$	Kronecker delta
$P_{\hat{L}}$	Probabilistic label map
A	Amplitude
$\mathcal{O}$	Offset
$\mathcal{S}(x)$	Step function
$g(x, s)$	Gaussian function
s	Standard deviation

Table 1 (continued)

Symbols	Descriptions
$\mathcal{E}(x)$	Ideal edge model
(x)	Blurred edge
I	2D isotropic Gaussian function
∇I_x and ∇I_y	Gradients along the X and Y directions
$\overline{D(x)}$	Sparse depth map
$D(x)$	Depth map
$\mathcal{L}$	Matting Laplacian factor
$\mathcal{M}$	Diagonal Matrix
λ	Scalar Balance factor
I	Skin lesion image
m_{kl}	Geometric moment
μ_{kl}	Central moment
η_{kl}	Higher order central moments
$\overline{x}$ and $\overline{y}$	Centers of gravity of image
m_{00}	Image quality
HM	Moment invariants of the Hu
AM_1, AM_2 *and A-* M_3	Affine moment invariants of first, second and third order
$\lvert V\rvert$	Total number of nodes
$\lvert L_i\rvert$	Length of the line segment L_i in the image
G	Streak graph
Density	Standard density of the graph 'G'
$Density_{streaks}$	Density measure of the streak graph
LesionSize	Size of the segmented lesion of the pixels
v_i	Vertex in the graph
G_w	Maximal connected subgraph
W	Largest connected subset
V	Vertex set
Z	Larger set
Completeness	Completeness of the pattern
$\lvert G_w\rvert$	Number of divided subgraphs in the image
y_i	Orientation
x_i	Valid streaks
β_0 and β_1	Intercept and slope of the regression line
e_i	Residual
$RMSE_d$	RMSE of the first derivation of orientations
$H(X)$	Entropy

Sink 't' is linked with Each pixel of Ω_B and $\Omega_{s,\,m,\,b}$. sink flow $p_i(x)$, $i \in B \cup L_2$ is defined.

- Within each image domain Ω_i, the pixel 'x' is quantified for spatial flow of $q_i(x)$, $i \in L_1 \cup L_2$.

Total flow running from source 's' to the sink 't' is maximed by the proposed HMF model.

$$\max_{p,q} \int_{\Omega} p_o(x)dx$$

Subjected to.

Flow capacity constraints: the sink flows $p_i(x)$, $i \in B \cup L_2$

$$p_i(x) \leq \rho_i(x), , i \in B \cup L_2 \tag{1}$$

and the spatial flows $q_i(x)$, $i \in L_1 \cup L_2$

$$|q_i(x)| \leq g(x), i \in L_1 \cup L_2 \tag{2}$$

Flow conservation constraints: In upper-level image domain, at each pixel the total flow residue disappearsΩ_i, $i \in L_1 = \{C, B\}$

$$G_i(x) := \left(div_{q_i} - p_o - p_i\right)(x) = 0, where\ i \in \{C, B\} \tag{3}$$

In bottom level image domain, at each pixel, the total flow residue vanishesΩ_i, where$i \in L_2 (= \{s, m, b\})$, i.e.,

$$G_i(x) := \left(div_{q_i} - p_c - p_i\right)(x) = 0, where\ i \in \{s, m, b\} \tag{4}$$

The source flow function $p_o(x)$ and blood flow function $p_c(x)$ are made free from the constraints by using the above definition. The Potts model is solved equally by calculating the HMF model. Flow conservation constraints are optimized using the labeling functions $u_i(x)$, *where* $i \in L_1 \cup L_2$ as the optimum multipliers. Direct confronting of the non-smooth total-variation functions is avoided using this HMF algorithm in the energy of Potts model. Flow configurations are adopted with labeling constraints.

At each k[th] iteration of HMF algorithm, the following steps are involved:

Spatial flows$|q_i(x)| \leq g(x)$, $i \in L_1 \cup L_2$, are minimized over $L_c(u; p, q)$, while fixing the other variables $(u; p)^k$ that amounts to

$$q_i^{k+1} := \underset{|q_i(x)| \leq g(x)}{\arg\max} -\frac{c}{2}\left\| divq_i - F_i^k \right\|^2 \tag{5}$$

Where $F_i^k(x), i \in L_1 \cup L_2$ is directly calculated from the fixed variables. This is calculated using the gradient projection iteration

$$q_i^{k+1} = Proj_{|q_i(x)| \leq g(x)}\left(q_i^k + \tau\nabla\left(divq_i^k - \left(F_i^k\right)\right)\right) \tag{6}$$

The above approximation converges if the step size $m > 0$ [39].

Source flow $p_o(x)$ is minimized over$L_c(u; p, q)$. Other variables $(u; p_i, q)^k$are fixed, that aggregates to

$$(p_o)^{k+1} := \arg\max_{p_0} \int_\Omega p_o dx - \frac{c}{2}\sum_{i \in \{B,C\}}\left\| p_o - J_i^k \right\|^2 \tag{7}$$

Where $J_i^k(x), i \in \{B, C\}$ is directly calculated from the fixed variables. This is solved exactly using

$$(p_o)^{k+1}(x) = \frac{\left(J_B^k(x) + J_C^k(x) + 1/c\right)}{2} \tag{8}$$

Maximize $L_c(u; p, q)$ over the blood flow $p_C(x)$, while fixing other variables $(u; p_o, p_{B,\ s,\ m,\ b}, q)^k$

$$(p_C)^{k+1} := \arg\max_{p_C} -\frac{c}{2}\sum_{i \in C \cup L_2}\left\| p_C - T_i^k \right\|^2 \tag{9}$$

Where $T_i^k(x), i \in C \cup L_2$ is directly calculated using the fixed variables. This is solved exactly using

$$(p_C)^{k+1}(x) = \frac{1}{4}\sum_{i \in C \cup L_2} T_i^k(x) \tag{10}$$

Maximize $L_c(u; p, q)$over $p_i(x) \leq \rho_i(x)$, $i \in B \cup L_2$, while fixing the variables $(u; p_o, p_c, q)^k$ that amounts to

$$(p_i)^{k+1} := \arg\max_{p_i(x) \leq \rho_i(x)} -\frac{c}{2}\left\| p_i - H_i^k \right\|^2 \tag{11}$$

Where $H_i^k(x), i \in B \cup L_2$ is directly calculated from the fixed variables. This is resolved accurately using

$$(p_i)^{k+1}(x) = \min\left(H_i^k(x), \rho_i(x)\right) \tag{12}$$

Labeling functions $u_i(x)$ are updated, where $i \in L_1 \cup L_2$, by

$$u_i^{k+1} = u_i^k - cG_i^k(x), where\ i \in L_1 \cup L_2 \tag{13}$$

Where $G_i^k(x), i \in L_1 \cup L_2$ represents the respective flow residue function [40].

B. *Patch-based label fusion model*

Sabuncu et al. [41] implemented a general fusion model and devised a Bayesian framework. The probabilistic patch-based model is implemented by extending this general model. Resultant voxels from the atlases of an image is used to create the voxel of each pixel in an image. Multi-atlas problem in a Bayesian framework is formulated by introducing one-on-one mapping from target voxel to atlas voxel. The posteriori probability can also be increased by using this method. The transformation from target voxel to voxel is validated by assuming the registration accuracy of an image. Image registration is flawless. The target voxel position is assumed as a transformed atlas position, if there is a mismatch between the target and wrapped image. The number of voxels in a local neighborhood in the atlas, is used to describe the registration error. If the computation of patch-based intensity similarity is greater than the computation using single voxel, voxels are replaced by patches. Atlas and target patches are related to decide the label in the target image. These labels are combined at last.

1) *Bayesian model*

In this model, the calculation of transformation Φ_n between the target image 'I' and atlas image I_n is assumed. Target space

is wrapped with the atlas image and its label map. Wrapped atlas image is represented by $I_n'(x) \equiv I_n(\Phi_n(x))$ and label map is represented by $L_n'(x) \equiv L_n(\Phi_n(x))$. Voxel $x + \Delta x$ in one of the warped atlas image is used to create the every voxel 'x'. Registration error between wrapped and target image is represented by Δx. Mapping of target voxel to voxel in the tlas is done by introducing the random vector filed $M : \Omega \rightarrow \{1, \ldots, N\} \times \{1, \ldots, K\}$. The number of candidate voxel in the local neighborhood is represented by 'K', where as 'N' denotes the number of atlases. Vector filed on the 3D lattice is represented by 'M'. The size of the vector is defined according to the target image. Mapping of voxel to atlas performed by first element of M(x) mapping of voxel to a candidate voxel is performed by second element. A $3 \times 3 \times 3$neighborhood centered at the voxel 'x' is used in the atlas image. 27 candidate voxels are present. Second atlas image is related to the target voxel 'x' and it is also related to the fifth candidate voxel. In this model, the index of an atlas is signified by the mapping M(x) for the voxel 'x'. It is a scalar quantity [42]. Voxel 'x' is mapped to a specific patch at an atlas by making this mapping operation as a vector one.

Label map 'L', image 'I' and atlas set $\{I_n', L_n' | n = 1, \ldots, N\}$ are estimated by segmentation process. It is estimated by Maximizing A Posteriori Probability (MAP) of the label map, which are trained on target image and atlas set

$$\hat{L} = \text{argmax}_L \, P\left(L \middle| I, \left\{I_n', L_n'\right\}\right) \tag{14}$$

Estimate of the label map 'L' is represented by $\hat{L}$. $P\left(L|I, \{I_n', L_n'\}\right)$ is constant and maximization is achieved by releasing it.

The joint probability can be written as,

$$P\left(I, L \middle| M, \left\{I_n', L_n'\right\}\right) = \prod_{x \in \Omega} P\left(I(x) \middle| M(x), \left\{I_n'\right\}\right) \cdot P\left(L(x) \middle| M(x), \left\{L_n'\right\}\right) \tag{15}$$

The joint probability is used for observing the target image and label map.

Target voxels are made independent by knowing the mapping field 'M'. The atlas voxels that are mapped to the target voxel determines the circulation of the target voxel. The intensity and label distributions are made conditionally independent by introducing the mapping filed 'M'. Intensity distribution of the mapped atlas voxel defines the intensity circulation of the voxel. Label map near atlas voxel defines the label distribution. The intensity and label distributions are conditionally independent. Analytical expression of the conditional probabilities $P(I(x)|M(x), \{I_n'\})$ and $P\left(L(x)|M(x), \{L_n'\}\right)$ are discussed in the below section.

Marginalization of the conditional probability is used to improve the probability of the label map.

$$P\left(I, L \middle| \left\{I_n', L_n'\right\}\right) = \sum_M P(M) \cdot \prod_{x \in \Omega} P\left(I(x) \middle| M(x), \left\{I_n'\right\}\right). \; P\left(L(x) \middle| M(x), \left\{L_n'\right\}\right) \tag{16}$$

2) *Intensity likelihood*

$M(x) = [M_1(x), M_2(x)]^T$Defines the mapping vector at voxel 'x'.M_1th atlas and M_2th candidate voxel are used to generate the target image voxel. Difference between target voxel and atlas voxel is due the effect of Gaussian noise. Let us assume M(x), the conditional probability of the intensity I(x) is expressed as

$$P\left(I(x) \middle| M(x), \left\{I_n'\right\}\right) = \frac{1}{\sqrt{2\pi\sigma_1}} \exp \left\{-\frac{1}{2\sigma_1^2}\left[I(x) - I_{M_1}'(x + \Delta_{M_2})\right]^2\right\} \tag{17}$$

Shift between M_2th candidate voxel and center voxel 'x' is represented by Δ_{M_2}. Intensity levels of target voxel and corresponding atlas voxel is given by $I(x)$and$I_{M_1}'(x + \Delta_{M_2})$. Standard deviation of the Gaussian noise is given by σ_1.

Due to the simplicity of the Gaussian distribution, an inordinate approximation of Rician distribution is calculated easily. Magnetic Resonance (MR) images noise intensity distribution follows the Rician distribution. Gaussian distribution is also suitable for obtaining higher signal to noise ratio [43]. Wrapping of the atlas image involves the image interpolation, which is used to estimate the noise present in each pixel. The non-uniformity and motion artifacts in the MR images are not considered.

Intensity likelihood on the small patch is calculated as,

$$P\left(I(x) \middle| M(x), \left\{I_n'\right\}\right) \approx \frac{1}{\sqrt{2\pi\sigma_1}} \exp \left\{-\frac{1}{2\sigma_1^2 |S(x)|} \times \left[I(y) - I_{M_1}'(y + \Delta_{M_2})\right]^2\right\} \tag{18}$$

The intensity likelihood is used to generate the robust estimate. Patch centered at voxel is represented by$S(x)$. Number of voxels in the patch is given by $|S(x)|$. Mean square variance in the patch S(x) replaces the intensity variance of a single voxel. As Gaussian distribution is followed by intensity variance at voxel $\left[I(x) - I_{M_1}'(x + \Delta_{M_2})\right]$, $\chi^2(S(n))$ distribution with S(n) degree of independence is followed by the mean squared variance. The growth in the S(n)makes the Gaussian distribution and normal distribution to meet asymptotically, as stated

by central limit theorem. Normal distribution is used to approximate the mean squared difference.

3) *Label likelihood*

Registration error between target image and wrapped atlas is calculated using label probability distribution. Due to this target patch corresponding to atlas patch interpreted. Registration error follows the normal distribution for simplification. Conditional probability of the label L(x) is expressed as

$$\mathrm{P}\left(\mathrm{L}(\mathrm{x})=\mathrm{l}\middle|\mathrm{M}(\mathrm{x}),\left\{\mathrm{L}_{\mathrm{n}}^{'}\right\}\right)$$

$$P(L(x))=\frac{1}{\sqrt{2\pi\sigma_2}}\exp\left\{-\frac{1}{2\sigma_2^2}|\Delta_{M_2}|^2\right\}\cdot\delta_{l,L_{M_1}}(x+\Delta_{M_2}) \quad (19)$$

Magnitude of shift vector Δ_{M_2} between atlas and target patch is represented by $|\Delta_{M_2}|$. Kronecker delta is represented by $\delta_{i,j}$. It will be equal to 0 when $i \neq j$. It is equal to one if $i = j$. Likelihood of the label is made non-zero by Kronecker delta. Large distance between the atlas patch gives less impact on the label.

A Markov Chain Monte Carlo (MCMC) is used for estimating the posterior distribution of the transformation that allows non-parametric modeling of the registration ambiguity that is computationally expensive [44, 45]. An approximate posterior distribution of transformation parameters is inferred using Variational Bayes [46, 47]. Multivariate normal distribution is followed by the transformation parameters. Weighted sum of the transformation parameters within its support region defines the displacement at each voxel. Normal distribution is followed by the registration error.

4) *MAP*

Let us assume that the mapping field $M(x)$ is uniformly distributed for all $x \in \Omega$

$$P(M(x))=\frac{1}{N^{|\Omega|}\cdot K^{|\Omega|}}, x\in\Omega \quad (20)$$

As a result, the posterior probability is maximized independently for each voxel

$$\hat{L}(x)=\mathrm{argmax}_l\sum_{M_1=1}^{N}\sum_{M_2=1}^{K}P\left(I(x)\middle|M(x),\left\{I_n^{'}\right\}\right). \quad (21)$$
$$P\left(L(x)=l\middle|M(x),\left\{L_n^{'}\right\}\right)$$

In weighted voting, 'N' atlas in the 'K' patch votes for label '1'. Transference between target patch and atlas patch and intensity similarity are used weight those votes. Label with high vote is selected. Local weighted fusion model is degenerated if K = 1 and it follows the model [48]. The registration errors are not considered. Each atlas is used to get the patch. Distance between the atlas and target patches defines the weight term. Non-local method is used for segmentation if the distance is not weighted and label likelihood is ignored [41, 49]. Thresholding of average label value is used to find the target label. It may be foreground or background. In the label fusion process, a probabilistic label map $\mathrm{P}_{\hat{\mathrm{L}}}$ is generated as

$$\mathrm{P}_{\hat{\mathrm{L}}}(\mathrm{x})=\left[\mathrm{P}_{\hat{\mathrm{L}},1}(\mathrm{x}),\mathrm{P}_{\hat{\mathrm{L}},2}(\mathrm{x}),\ldots,\mathrm{P}_{\hat{\mathrm{L}},\mathcal{L}}(\mathrm{x})\right]^{\mathrm{T}} \quad (22)$$

Where the probabilistic vector at the voxel 'x' is represented by $\mathrm{P}_{\hat{\mathrm{L}}}(\mathrm{x})$, lth element of the vector $\mathrm{P}_{\hat{\mathrm{L}},\mathcal{L}}(\mathrm{x})$ indicates the probability to the lth class. The probabilistic label map is used for the refinement of image registration.

C. *Feature Extraction*

1) *3D depth feature*

Three-Dimensional (3D) reconstruction estimates the skin lesion depth. Active illumination and coded aperture image acquisition methods are used to estimate the depth of the skin lesion. In [42], a single image is acquired from the unrestricted image [50, 51] acquisition technique for estimating the depth.

Reconstruction of 3D surface represented by structure tensors are enabled by the depth map of the two dimensional surface. Defocus at the edge occurrence is used to compute the depth of the skin. A Gaussian function reblurs the input skin lesion images. Defocus at the edge is computed as a ratio of gradient magnitude of input skin lesion image and reblurred image. Depth maps are computed by spreading the blur in the edge over an image. Step model is placed at the edge is given by

$$\varepsilon(x)=A\mathcal{S}(x)+\mathcal{O} \quad (23)$$

Amplitude is represented by 'A'. Offset is denoted by '$\mathcal{O}$', step function is given by '$\mathcal{S}(x)$'. Convoluting the sharp input skin image with a point spread function, defocus blur is obtained. The point spread function is approximated using Gaussian function. Circle of confusion 'c' is linearly proportional to the standard deviation of the Gaussian function and it is given by,

$$s=\|c \quad (24)$$

Gaussian function and ideal edge model is multiplied to get the blurred edge $(x)$and it is given by,

$$\mathcal{B}(x)=\mathcal{E}(x)\otimes g(x,s) \quad (25)$$

Input skin image is denoted by 'I'. Input image is re-blurred by applying two-dimensional isotropic Gaussian function I. Gradient magnitude is given by

$$\|\nabla I(x,y)\| = \sqrt{\nabla I_x^2 + \nabla I_y^2} \tag{26}$$

Gradient along X and Y directions are given by $\nabla I_x$and ∇I_y. In the same way gradient magnitude of blurred image is also calculated. $\frac{\|\nabla I(x)\|}{\|\nabla I^B(x)\|}$ defines the ratio of gradient between the edge locations of the input image and isotropic Gaussian function. Occurrence of blur scale at the edge location is estimated to generate the sparse depth map $D(x)$. Joint bilateral filter and input image as a reference, wrong blur approximations are removed.

Defocus blur estimates calculated over entire image are transmitted to obtain the full depth map $D(x)$. The $D(x)$ is also used to get the full depth map. Matting Laplacian technique [43] is used to get the full depth map. Matting Laplacian technique is a interpolation method. The following equation is solved to get the optimal depth map 'D'.

$$(\mathcal{L} + \lambda\mathcal{M})D = \lambda\mathcal{M}\overline{D} \tag{27}$$

Matting Laplacian factor is given by '$\mathcal{L}$ '. Diagonal matrix is given by $\mathcal{M}$, scalar balance is given by 'λ'. Full depth map and spare depth map is denoted by D and $\overline{D}$.

Features like maximum depth, minimum depth and relative depth are extracted from the 3D skin lesion. 3D shape features of skin lesion are characterized by three affine moment invariants [52] and Seven Hu invariants [53]. The geometric moment of a skin lesion image 'I' with size $K \times L$ is given by

$$m_{kl} = \sum_{x=0}^{K-1}\sum_{y=0}^{L-1} f(x,y)x^k y^l \tag{28}$$

The $(k+l)^{th}$ order central moment is

$$\mu_{kl} = \sum_{x=0}^{K-1}\sum_{y=0}^{L-1} f(x,y)\left(x-\overline{x}\right)^k\left(y-\overline{y}\right)^l \tag{29}$$

Where $\overline{x} = m_{10}/m_{00}$ and $\overline{y} = m_{01}/m_{00}$ are the center of gravity of an image m_{00}. m_{00}represents the quality, while considering the intensity images. The shape of the image is represented by the geometric and central moments $m_{kl}$and μ_{kl}.

The higher order central moments is normalized using the 0^{th} order central moment

$$\eta_{kl} = \frac{\mu_{kl}}{\mu_{00}^r} \tag{30}$$

Where $r = \frac{k+l+2}{2}$ and $k+l = 2, 3, 4, \ldots\ldots$

The moment invariants of the Hu are calculated as

$$HM_1 = \eta_{20} + \eta_{02} \tag{31}$$

$$HM_2 = (\eta_{20}-\eta_{02})^2 + 4\eta_{11}^2 \tag{32}$$

$$HM_3 = (\eta_{30}-3\eta_{12})^2 + (3\eta_{21}-\eta_{02})^2 \tag{33}$$

$$HM_4 = (\eta_{30} + \eta_{12})^2 + (\eta_{21} + \eta_{03})^2 \tag{34}$$

$$HM_5 = (\eta_{30}-3\eta_{12})\Big((\eta_{30} + \eta_{12})\Big[(\eta_{30} + \eta_{12})^2-2(\eta_{21} + \eta_{03})^2\Big]\Big) + (\eta_{30}-3\eta_{21})\Big((\eta_{03} + \eta_{21}) \times \Big[(\eta_{03} + \eta_{21})^2-2(\eta_{12} + \eta_{30})^2\Big]\Big) \tag{35}$$

$$HM_6 = \Big((\eta_{20}-\eta_{02})\Big[(\eta_{30} + \eta_{12})^2-(\eta_{21} + \eta_{03})^2\Big]\Big) + (4\eta_{11}(\eta_{30} + \eta_{12})(\eta_{21} + \eta_{03})) \tag{36}$$

$$HM_7 = \Big((3\eta_{21}-\eta_{03})(\eta_{30} + \eta_{12})\Big[(\eta_{30} + \eta_{12})^2-3(\eta_{21} + \eta_{03})^2\Big]\Big) -\Big((3\eta_{12}-\eta_{30})(\eta_{03} + \eta_{21}) \times \Big[(\eta_{03} + \eta_{21})^2-3(\eta_{12} + \eta_{30})^2\Big]\Big) \tag{37}$$

3D shape features are given by the first, second and third order of the affine moment invariants and it is given by [52],

$$AM_1 = \left(\mu_{20}\mu_{02}-\mu_{11}^2\right)/\mu_{00}^4 \tag{38}$$

$$AM_2 = \left(\mu_{30}^2\mu_{03}^2-6\mu_{30}\mu_{21}\mu_{12}\mu_{03} + 4\mu_{30}\mu_{12}^3 + 4\mu_{21}^3\mu_{03}-3\mu_{21}^2\mu_{12}^2\right)/\mu_{00}^{10} \tag{39}$$

$$AM_3 = \mu_{20}\left(\mu_{12}\mu_{03}-\mu_{12}^2\right)-\mu_{11}\left(\mu_{30}\mu_{03}-\mu_{21}\mu_{12}\right) + \mu_{02}\left(\mu_{30}\mu_{12}-\mu_{21}^2\right)/\mu_{00}^7 \tag{40}$$

2) *Lesion Color Texture (LCT) – Streax (STR) features*

LCT

Features like mean, standard deviation, texture measures like energy, contrast, correlation are involved in the LCT. Texture features are computed by Grey Level Co-occurrence Matrix (GLCM). Occurrence probability of pair of pixels in an image is tabulated using GLCM [14].Green plane is used to compute the green features.

Missing information in the lesion is computed by the LCT. Border irregularity, asymmetry and color counts features are included in the LCT. Modeling of streak patterns are assisted by LCT.

STR

Modeling the characteristics of absent, regular and irregular streaks are done by STR. It is a mathematical function and defined by oriental pattern analysis.

3) *Geometric graph features*

In the detection of irregularity, uniformity and smoothness of the orientation change plays a vital role. Fullness of the pattern is represented by connectivity of the structure. Pigment Network (PN) defines the dermoscopy structure, which is represented by density ratio features [54]. Density of the streaks on the image is measured with some modifications. Present images are differentiated from absent images by using this modification. Valid streak lines are created by reducing each line. Total number of nodes is given by,

$$|V| = \sum_{i=1}^{N} \left(\left(\frac{|L_i|}{\sum_{j=1}^{N} |L_j|/N} \right) + 1 \right) \tag{41}$$

The length of the line segment L_i is given by $|L_i|$. Average length of the streaks is given by $\sum_{j=1}^{N} |L_j|/N$. Longer streak lines will have high influence in future calculations and shorter lines will have only one node in the streak graph 'G'.

Density ratio: A graph with vertices $v \in V$ and edges $E \subseteq (V \times V)$ is defined and its standard density is defined by,

$$Density = \frac{2 \times |E|}{|V| \times (|V|-1)} \tag{42}$$

Number of vertices in the graph is defined by the ration of edges in the graph to the possible number of edges. Density measure is given by,

$$Density_{streaks} = \frac{|E|(log|E|)}{|V| \times log(LesionSize)} \tag{43}$$

Size of the segmented lesion of the pixels is given by *LesionSize*. Present and absent images are differentiated by density features. Regularity, abnormality, completeness and coverage of the pattern are not defined by this density measure.

The lesion consists of a comprehensive pattern which is of high density. In case of irregular streaks, the graph is dense around the small area. Distribution of the dense pattern requires another parameter to find out. For this purpose, completeness and pattern coverage are used.

Streak pattern coverage

Number of streaks in different areas of lesion are calculated to find the histogram of streaks. Streaks are defined as the linear structures that are co-radially oriented over the boundary. The coverage of the graph ranges from 0 to 1. It is defined by the bins with more than two streak lines. Its optimal value is 1. This optimal value indicates the symmetrical distribution of streaks. Asymmetrical streaks has partial distribution pattern.

Completeness

The graph is said to be connected if each vertex is reachable from other vertex. The completeness is given by,

$$Completeness = \frac{Density_{streaks}}{|G_w|} \tag{44}$$

The number of disconnected sub-graphs in the image is denoted by $|G_w|$.

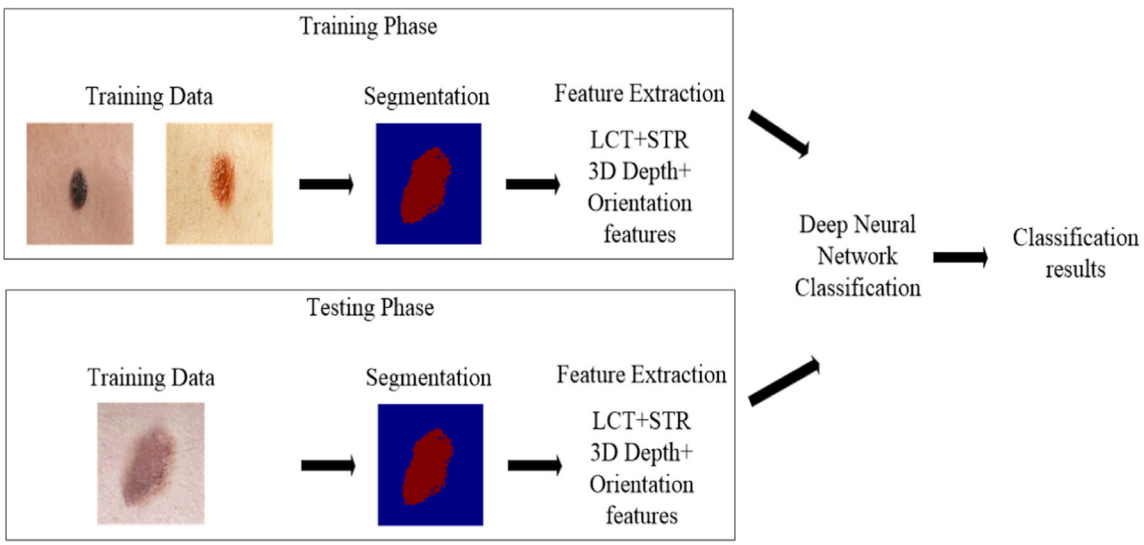

Fig. 2 System architecture of the proposed work

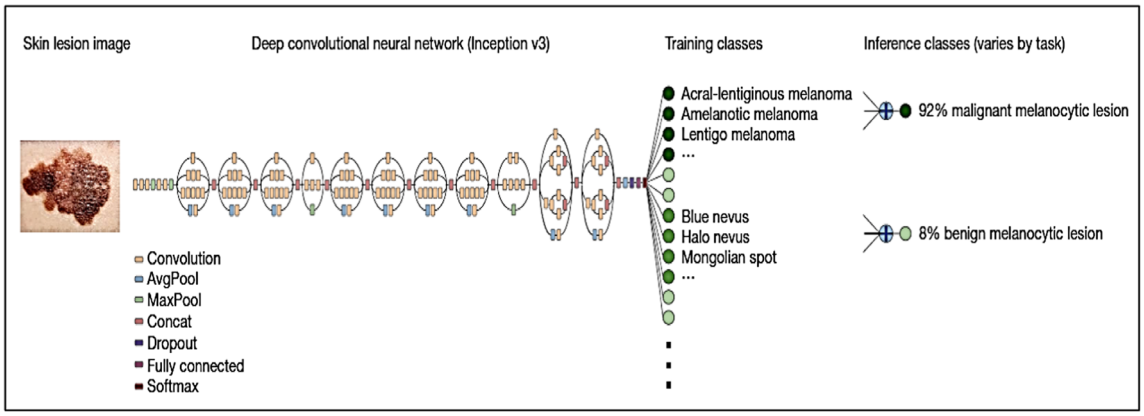

Fig. 3 Deep CNN layout architecture

4) *Orientation features*

The presence, abnormality and regularity of the streaks can also be found by the orientation information. Change in the orientation of the streaks are used to get the original pattern. The location and the orientation from the major axis are used to order the line segments. Regular streaks consist of smooth orientation variation. They don't have any major jumps between data points. The error is measured by applying the linear regression on the ordered line segments, as they are oriented co-radially. Regularity and asymmetry features are extracted. It is assumed that the ordered valid streaks x_i where 'i' ranging from 1 to N and y_i denotes the corresponding orientation. In linear regression y_i is expressed as

$$\hat{y_i} = \beta_0 + \beta_1 x_i \;\; for\; i = 1, \ldots\ldots, N \tag{45}$$

Intercept and slope of the regression line is given by $\beta_0$and β_1. The residual e_i defines the difference between predicted and actual direction.

Root Mean Square Error (RMSE) is given by,

$$RMSE = \sqrt{\frac{\sum_i (\hat{y_i} - y_i)^2}{N}} \tag{46}$$

Large number of streaks in the X-axis corresponds to low RMSE and lower slope of β_1. It corresponds to theimages with regular streaks. The RMSE of the first derivation of orientations is given by

$$RMSE_d = \sqrt{\frac{\sum_i (\hat{y_i} - y_i')^2}{N}} \tag{47}$$

The derivative of $\hat{y}_i$ *and* y_i is given by $\hat{y_i}$ and y_i'.

The lines outside the predefined range are called as outlier. The range is given by +30 degrees or − 30 degrees. They are located outside the fit line. Line segments are used to regularize the outliers.

Patterns in the orientation variations are characterized by the entropy of the line variation and its residuals. Uncertainty is defined by the entropy. High entropy is given by irregular streaks and regular streaks gives less entropy value. The entropy is given by,

$$H(X) = -\sum_{i=1}^{n} p(x_i) log_b p(x_i) \tag{48}$$

The probability function of x_i is given by $p(x_i)$and contains the histogram counts of 'b' bins where $b = \frac{2\pi}{\pi/18} = 36$.

5) *Chromatic features of streaks*

streak lines are detected by using color features like mean and standard deviation. The choice of color channel and HSV color space is also used for this purpose.

Fig. 4 Input Image

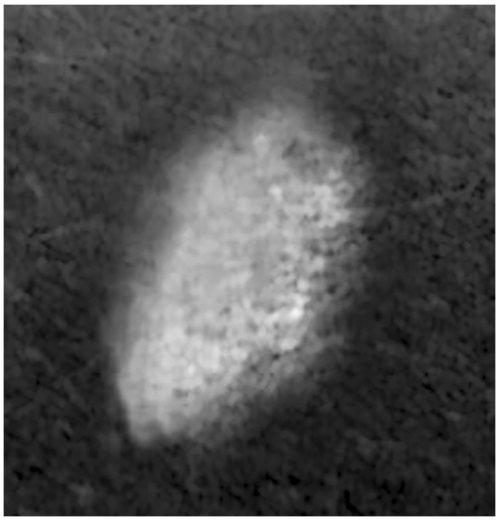

Fig. 5 Preprocessed Image

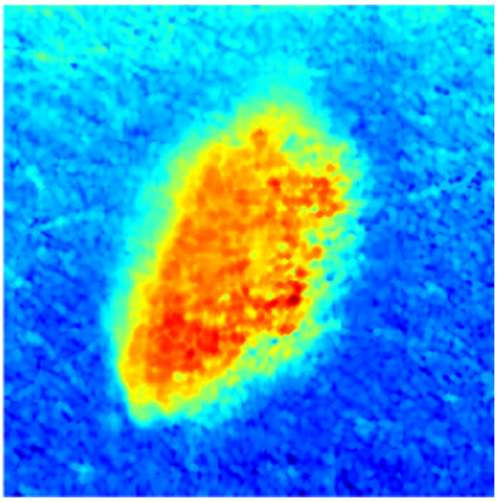

Fig. 7 Atlas Map

D. *Structural features*

Structural features like shape, variability of the lines and length are used for segmentation streaks. The number of pixels in a line segment is calculated. Features like mean value and total streaks are used for segmentation.

E. *Classification*

Input skin lesions are classified using Deep Neural Network (DNN). Deep neural network takes the 3D depth features and LCT and STR features as input. Class label for true skin lesion 'y' predicted using DNN. The classification of disease into different classes is done by an algorithm. CNN outputs a probability distribution over these fine classes. Proposed system architecture is shown in Fig. 2. Architecture layout of CNN is shown in Fig. 3.

The GoogleNet Inception v3 CNN architecture [55] is applied in our work. The CNN is trained using the back propagation. All layers of the network are fine-tuned by using the same global learning rate of 0.001 and a decay factor of 16 each 30 epochs. A two-layer convolutional architecture is used. The first layer in the architecture is a 3×3 convolution, the second layer is a fully connected layer on the top of the 3×3 output grid of the first layer. The 5×5 convolution is replaced with two layers of 3×3 convolution while sliding this small network over the input activation grid. The parameter count is reduced by sharing the weights between adjacent tiles. The number of activations/unit is changed by a constant alpha factor α. As the 5×5 convolution is combined, the alpha factor is somewhat larger than one. A two-layer replacement for the 5×5 layer is reasonable by increasing the number of filters. Network sliding is represented using two 3×3 convolutional layers that reuse the activations between the

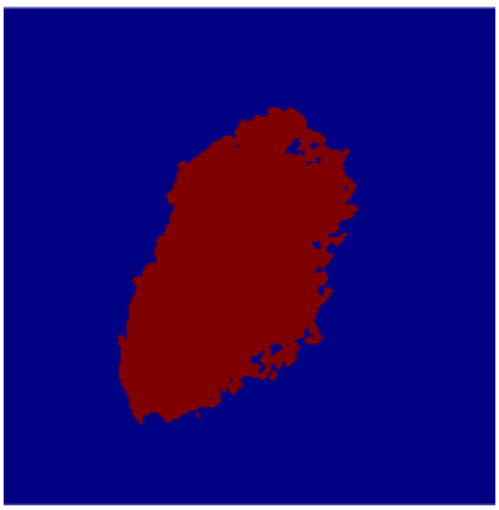

Fig. 6 HMF segmented image

Fig. 8 Patch-based Label Fusion Image

adjacent tiles. An average pooling layer performs down-sampling process by dividing the input into rectangular pooling regions and computing the average values of each pooling region. Max pooling is a sample-based discretization process applied to down-sample an input representation while reducing its dimensionality and allowing the assumptions about the features contained in the binned sub-regions. The Concat layer is a utility layer that concatenates its multiple input blobs to a single output blob. Dropout is a regularization technique used for reducing overfitting in the neural networks by preventing complex co-adaptations on training data. With the fully connected layers, the features are combined together to create a model. The softmax function compresses the outputs of each unit to be between 0 and 1. The output of the softmax function is equal to a definite probability distribution that states the probability that any of the classes are true.

Convolutions with the filters larger 3×3 are not useful as they can always be reduced into a sequence of 3×3 convolutional layers. The two-layer solution is cheaper for the same number of output filters, if the number of the input and output filters is equal. By comparison, a 3×3 convolution is factorized into a two 2×2 convolution while saving the computational requirement. Softmax activation function is applied as it is highly useful because it converts the output of the last layer in the neural network into an essential probability distribution that states whether any of the classes are true.

Performance analysis

The performance of the proposed work is simulated using the MATLAB software and compared with the patch-based label fusion model [48] and 3D reconstruction technique [56]. The performance analysis is evaluated using the PH2 [57] and Atlas databases [58]. The PH2 database from the Pedro Hispano hospital is used for evaluation. About 200 images are used for this purpose. All images in the PH2 database

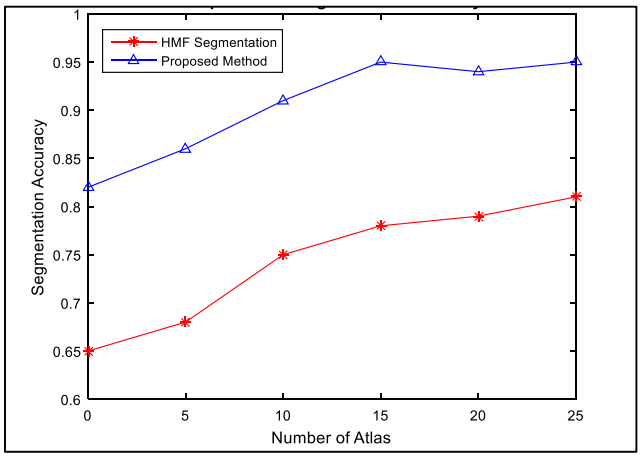

Fig. 9 Effect of the size of atlas subset on segmentation accuracy

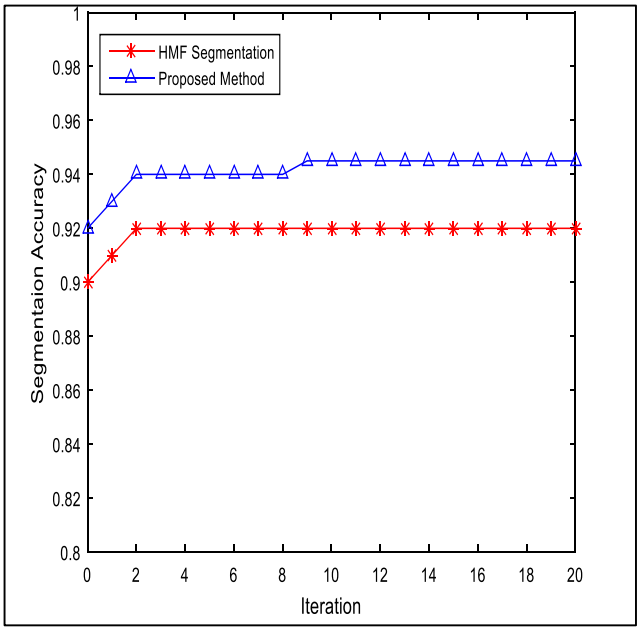

Fig. 10 Effect of the iterative registration refinement on segmentation accuracy evaluated using the Dice metric

are 8-bit RGB color images. There are four types of classes including common nevus, atypical nevus, melanoma and in-situ melanoma considered in the PH2 database. The proposed work is evaluated by ATLAS databases which consist of all the set of skin lesion images. This dataset considers 8 types of skin lesions. The color and texture information is insufficient to classify the skin lesions as shown by the ATLAS dataset. The ATLAS dataset comprises a complete set of skin lesion images to evaluate the proposed work. The ATLAS dataset considers 8 types of skin lesions. ATLAS dataset show that the color and texture information is insufficient to classify the skin lesions.Figure.4 shows the input image and Fig. 5 depicts the preprocessed image. The HMF segmented image is presented in Fig. 6 and atlas map is illustrated in Fig. 7. Figure.8 shows the patch-based label fusion image.

The Segmentation accuracy between manual label maps and automated segmentation techniques are measured by Dice overlap. Figure.9 shows the relationship between

Table 2 Experiment details using various feature types and datasets

Dataset used	Features selected	Notation
PH^2 [57]	2D and 3D shapes	D1EX1
PH^2 [57]	Color, Texture	D1EX2
PH^2 [57]	Color, Texture, 2D shape	D1EX3
PH^2 [57]	Color, Texture, 2D and 3D shapes	D1EX4
ATLAS [58]	2D and 3D shapes	D2EX1
ATLAS [58]	Color, Texture	D2EX2
ATLAS [58]	Color, Texture, 2D shape	D2EX3
ATLAS [58]	Color, Texture, 2D and 3D shapes	D2EX4

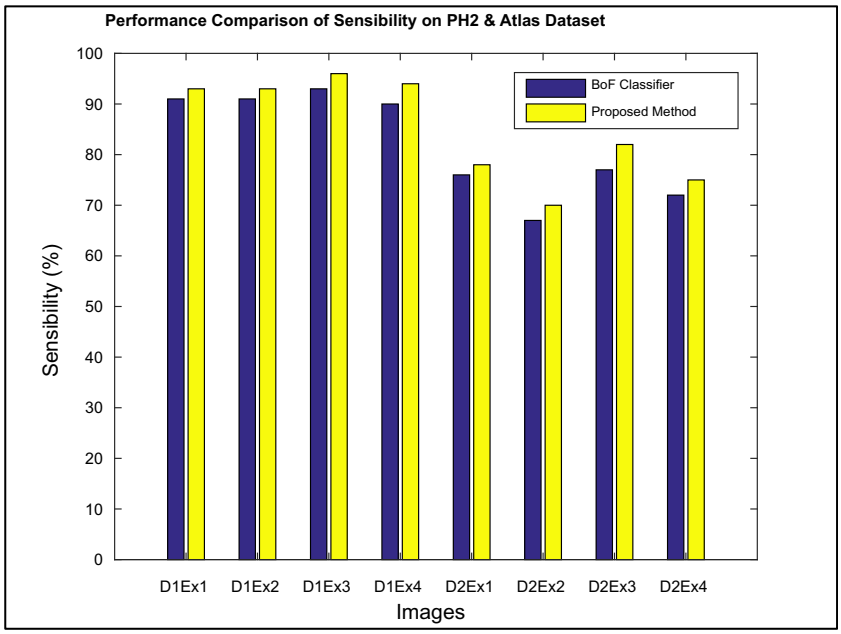

Fig. 11 Sensibility analysis on the PH^2 and Atlas databases

segmentation accuracy and size of the atlas subset. The increase in the number of atlas maps linearly increases the accuracy of the segmentation. The Segmentation accuracy of the proposed method is high when compared to the HMF method.

The registration process is initiated by giving label information. Cost function is changed a lot by the updated label map. Registration process is repeated in all iterations. Due to its computational expensiveness, only one iteration is enough to get the accurate results. The algorithm may converge after six iterations due to change in the label map. Effect of iteration registration refinement is shown in Fig. 10. The segmentation accuracy of the proposed method is higher than the HMF segmentation.

The performance of the proposed work is evaluated by cost function, which is based on the confusion matrix. Specificity (SP) and sensibility (SE) values are used evaluate the cost function as,

$$\mathcal{C} = \frac{\mathcal{K}_{FN}(1-SE) + \mathcal{K}_{FP}(1-SP)}{\mathcal{K}_{FN} + \mathcal{K}_{FP}} \tag{49}$$

Where False Positive (FP) cost is represented by$\mathcal{K}_{FN}$, and False Negative (FN) cost is represented by $\mathcal{K}_{FP}$.Various

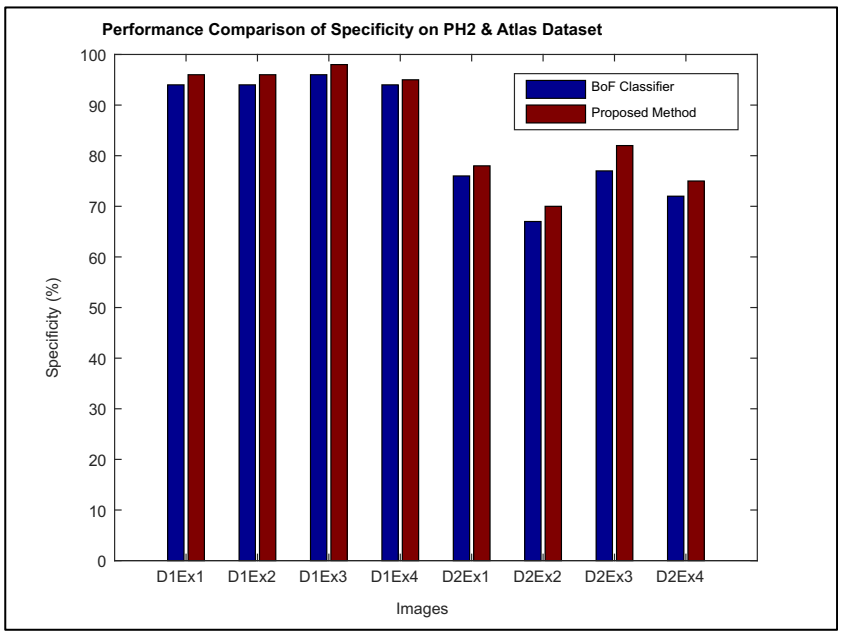

Fig. 12 Specificity analysis on the PH^2 and Atlas databases

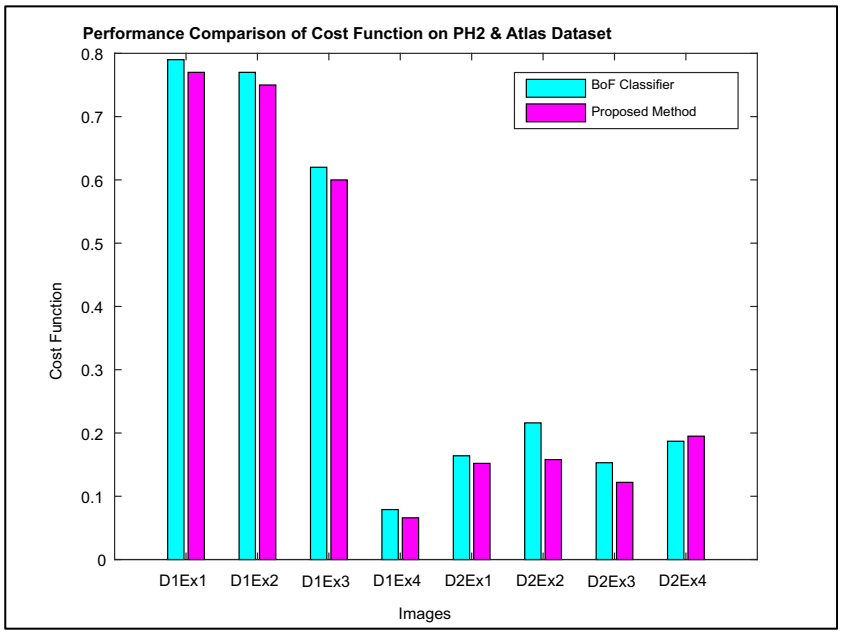

Fig. 13 Cost function analysis on the PH^2 and Atlas databases

feature types and datasets are used for experimentation as shown in Table 2. Figure.11 illustrates the sensibility analysis on the PH2 and Atlas databases. Figure.12 presents the specificity analysis on the PH2 and Atlas databases. The proposed method yields maximum sensibility and specificity than the BoF classifier. Figure.13 shows the cost function analysis on the PH2 and Atlas databases. The proposed method requires minimum cost function than the BoF classifier.

The efficiency of the proposed work is evaluated using two image sets of 945 and 375. The evaluation results are shown in Table 2. Some of the images in the sets are challenging due to the lighting and magnification parameters, or due to the presence of occlusion such as oil or hair. The results of the four set of features such as LCT, STR, LCT + STR and LCt + STR + 3DDepth + Orientation into three classes including Absence/Presence, Regular/Irregular and Absence/Regular/Irregular are reported in Table 3. Three different resources are used to collect the first set of 945 dermoscopic images (570 Absent, 245 Irregular, and 130 Regular). Based on the regularity of the streaks in the image the, the images are labeled as Absent, Regular or Irregular. Interactive atlas of dermascopy is used to collect the 745 images in the first subset [59]. Web is used to collect 100 Regular or Irregular streaks images. Atlas of pigmented skin lesions is used to take [60] third subset of 100 images with Absent, Regular or Irregular labels. The proposed LCT + STR + 3DDepth + Orientation features outperformed the existing LCT, STR and LCT + STR in terms of various performance measures as shown in Table 2.

Table 3 Evaluation of proposed method with two image datasets

Experiment	Total Images	Features	Precision	Recall	F-measure	Accuracy	AUC
Absence/Presence	945	LCT	0.666	0.672	0.652	0.670	0.7
		STR	0.751	0.754	0.751	0.755	0.802
		LCT + STR	0.780	0.782	0.780	0.783	0.832
		LCT + STR + 3D Depth + Orientation	0.925	0.90	0.917	0.947	0.928
Regular/Irregular	375	LCT	0.729	0.736	0.731	0.736	0.8
		STR	0.786	0.792	0.785	0.791	0.849
		LCT + STR	0.834	0.836	0.834	0.836	0.889
		LCT + STR + 3D Depth + Orientation	0.93	0.915	0.92	0.951	0.934
Absence/Regular/Irregular	945	LCT	0.615	0.630	0.590	0.640	0.741
		STR	0.671	0.69	0.670	0.7	0.791
		LCT + STR	0.744	0.76	0.742	0.761	0.85
		LCT + STR + 3D Depth + Orientation	0.928	0.922	0.935	0.96	0.936

Conclusion

Majority of death is due to the melanoma among most the skin cancers. It is possible to cure it easily if it detected at the earliest. Dermoscopic techniques are used for diagnosis of skin lesion. Depth of the melanoma tumor is essential. This is not done by the existing methods effectively. 2D surface is used to find the depth map, which is used for 3D reconstruction. Streaks lines are to be detected and segmented for extracting features. Additional flows are used HMF to encode the specified region. Melanoma is easily curable if it is diagnosed in the earlier stages. Using non-invasive computer-based dermoscopy methods, skin lesion diagnosis is commonly adopted. The depth of the melanoma tumor into the skin is to be identified in order to determine the stage of melanoma. Existing dermoscopy techniques place minimal or no emphasis on the depth analysis for the melanoma diagnosis. The 3D image reconstruction is achieved by fitting the depth map assessed to the underlying 2D surface. The low contrast and fuzzy streak lines are detected and the detected segments are used for extracting the clinically inspired feature sets for the orientation analysis of the structure. The HMF model indirectly encodes the definite region order or layout by the additional flows. This avoids confronting the challenging region order constraint clearly. The experimental results have proven the ability of the proposed algorithm in segmentation and classification process. From the experimental results, it is concluded that the proposed method provides maximum segmentation, sensibility, specificity and minimum cost function than the existing segmentation technique and classifier. In future, depth estimation error is to be identified using the clinical data and new techniques are developed to reduce errors. Also, the segmented line segments will be investigated more locally and accurately, by carefully analyzing the shape of lesions and fitting multiple ellipses.

Compliance with Ethical Standards

Conflict of Interest The authors have no conflict of interests and the paper has not been submitted to any other Journals.

Research Involving Human Participants and/or Animals This article does not contain any studies with human participants or animals performed by any of the authors.

Informed Consent It is not required as the dataset is taken online databases.

References

1. Menzies, S. W., Ingvar, C., Crotty, K. A., and McCarthy, W. H., Frequency and morphologic characteristics of invasive melanomas lacking specific surface microscopic features. Arch. Dermatol. 132: 1178–1182, 1996.
2. Argenziano, G., Fabbrocini, G., Carli, P., De Giorgi, V., Sammarco, E., and Delfino, M., Epiluminescence microscopy for the diagnosis of doubtful melanocytic skin lesions: Comparison of the ABCD rule of dermatoscopy and a new 7-point checklist based on pattern analysis. Arch. Dermatol. 134:1563–1570, 1998.
3. Stolz, W., ABCD rule of dermatoscopy: A new practical method for early recognition of malignant melanoma. Eur. J. Dermatol. 4:521–527, 1994.
4. Blum, A., Rassner, G., and Garbe, C., Modified ABC-point list of dermoscopy: A simplified and highly accurate dermoscopic algorithm for the diagnosis of cutaneous melanocytic lesions. J. Am. Acad. Dermatol. 48:672–678, 2003.
5. Barata, C., Ruela, M., Francisco, M., Mendonça, T., and Marques, J. S., Two systems for the detection of melanomas in dermoscopy images using texture and color features. IEEE Syst. J. 8:965–979, 2014.
6. Pereyra, M. A., Dobigeon, N., Batatia, H., and Tourneret, J.-Y., Segmentation of skin lesions in 2D and 3D ultrasound images using a spatially coherent generalized Rayleigh mixture model. IEEE Trans. Med. Imaging 31:1509–1520, 2012.
7. Steiner, A., Binder, M., Schemper, M., Wolff, K., and Pehamberger, H., Statistical evaluation of epiluminescence microscopy criteria for melanocytic pigmented skin lesions. J. Am. Acad. Dermatol. 29: 581–588, 1993.
8. Sadeghi, M., Lee, T. K., McLean, D., Lui, H., and Atkins, M. S., Detection and analysis of irregular streaks in dermoscopic images of skin lesions. IEEE Trans. Med. Imaging 32:849–861, 2013.
9. Heckemann, R. A., Hajnal, J. V., Aljabar, P., Rueckert, D., and Hammers, A., Automatic anatomical brain MRI segmentation combining label propagation and decision fusion. NeuroImage 33:115–126, 2006.
10. Rohlfing, T., Russakoff, D. B., and Maurer, C. R., Performance-based classifier combination in atlas-based image segmentation using expectation-maximization parameter estimation. IEEE Trans. Med. Imaging 23:983–994, 2004.
11. Rohlfing, T., Brandt, R., Menzel, R., and Maurer, Jr., C. R., Evaluation of atlas selection strategies for atlas-based image segmentation with application to confocal microscopy images of bee brains. NeuroImage 21:1428–1442, 2004.
12. Svarer, C., Madsen, K., Hasselbalch, S. G., Pinborg, L. H., Haugbøl, S., Frøkjær, V. G. et al., MR-based automatic delineation of volumes of interest in human brain PET images using probability maps. Neuroimage 24:969–979, 2005.
13. Abuzaghleh, O., Barkana, B. D., and Faezipour, M., Noninvasive real-time automated skin lesion analysis system for melanoma early detection and prevention. IEEE J. Trans. Eng. Health Med. 3:1–12, 2015.
14. Glaister, J., Wong, A., and Clausi, D. A., Segmentation of skin lesions from digital images using joint statistical texture distinctiveness. IEEE Trans. Biomed. Eng. 61:1220–1230, 2014.
15. M. H. Jafari, N. Karimi, E. Nasr-Esfahani, S. Samavi, S. M. R. Soroushmehr, K. Ward, *et al.*, "Skin lesion segmentation in clinical images using deep learning," in *Pattern Recognition (ICPR), 2016 23rd International Conference on*, 2016, pp. 337-342.
16. Peruch, F., Bogo, F., Bonazza, M., Cappelleri, V.-M., and Peserico, E., Simpler, faster, more accurate melanocytic lesion segmentation through meds. IEEE Trans. Biomed. Eng. 61:557–565, 2014.
17. Ma, Z., and Tavares, J. M. R., A review of the quantification and classification of pigmented skin lesions: From dedicated to hand-held devices. J. Med. Syst. 39:177, 2015.
18. Navarro, F., Escudero-Vinolo, M., and Bescos, J., Accurate segmentation and registration of skin lesion images to evaluate lesion change. IEEE J. Biomed. Health Inform., 2018.
19. Dhawan, A. P., Gordon, R., and Rangayyan, R. M., Nevoscopy: Three-dimensional computed tomography of nevi and melanomas

in situ by transillumination. IEEE Trans. Med. Imaging 3:54–61, 1984.
20. Tittmann, B. R., Miyasaka, C., Maeva, E., and Shum, D., Fine mapping of tissue properties on excised samples of melanoma and skin without the need for histological staining. IEEE Trans. Ultrason. Ferroelectr. Freq. Control 60:320–331, 2013.
21. Vogt, M., and Ermert, H., In vivo ultrasound biomicroscopy of skin: Spectral system characteristics and inverse filtering optimization. IEEE Trans. Ultrason. Ferroelectr. Freq. Control 54, 2007.
22. Kaur, G., and Joshi, K., Automatic detection and segmentation of skin melanoma images-an introduction. Int. J. Emerg. Res. Manag. Technol. ISSN:2278–9359, 2015.
23. Esteva, A., Kuprel, B., Novoa, R. A., Ko, J., Swetter, S. M., Blau, H. M. et al., Dermatologist-level classification of skin cancer with deep neural networks. Nature 542:115, 2017.
24. Menzies, S., Ingvar, C., and McCarthy, W., A sensitivity and specificity analysis of the surface microscopy features of invasive melanoma. Melanoma Res. 6:55–62, 1996.
25. Kasmi, R., Mokrani, K., Rader, R., Cole, J., and Stoecker, W., Biologically inspired skin lesion segmentation using a geodesic active contour technique. Skin Res. Technol. 22:208–222, 2016.
26. Pennisi, A., Bloisi, D. D., Nardi, D., Giampetruzzi, A. R., Mondino, C., and Facchiano, A., Skin lesion image segmentation using Delaunay triangulation for melanoma detection. Comput. Med. Imaging Graph. 52:89–103, 2016.
27. N. Mittal, S. Tanwar, and S. K. Khatri, "Identification & enhancement of different skin lesion images by segmentation techniques," in *Reliability, Infocom Technologies and Optimization (Trends and Future Directions)(ICRITO), 2017 6th International Conference on*, 2017, pp. 609-614.
28. B. Patel, K. Dhayal, S. Roy, and R. Shah, "Computerized skin cancer lesion identification using the combination of clustering and entropy," in *Big Data Analytics and Computational Intelligence (ICBDAC), 2017 International Conference on*, 2017, pp. 46–51.
29. Ma, Z., and Tavares, J. M. R., A novel approach to segment skin lesions in dermoscopic images based on a deformable model. IEEE J. Biomed. Health Inform. 20:615–623, 2016.
30. L. Bi, J. Kim, E. Ahn, D. Feng, and M. Fulham, "Automated skin lesion segmentation via image-wise supervised learning and multi-scale superpixel based cellular automata," in *Biomedical Imaging (ISBI), 2016 IEEE 13th International Symposium on*, 2016, pp. 1059-1062.
31. A. A. A. Al-abayechi, H. A. Jalab, R. W. Ibrahim, and A. M. Hasan, "Image Enhancement Based on Fractional Poisson for Segmentation of Skin Lesions Using the Watershed Transform," in *International Visual Informatics Conference*, 2017, pp. 249-259.
32. S. Ross-Howe and H. R. Tizhoosh, "The Effects of Image Pre-and Post-Processing, Wavelet Decomposition, and Local Binary Patterns on U-Nets for Skin Lesion Segmentation," in *2018 International Joint Conference on Neural Networks (IJCNN)*, 2018, pp. 1-8.
33. Li, Y., and Shen, L., Skin lesion analysis towards melanoma detection using deep learning network. Sensors 18:556, 2018.
34. N. C. Codella, D. Gutman, M. E. Celebi, B. Helba, M. A. Marchetti, S. W. Dusza, *et al.*, "Skin lesion analysis toward melanoma detection: A challenge at the 2017 international symposium on biomedical imaging (isbi), hosted by the international skin imaging collaboration (isic)," in *2018 IEEE 15th International Symposium on Biomedical Imaging (ISBI 2018)*, 2018, pp. 168-172.
35. A. R. Jadhav, A. G. Ghontale, and V. K. Shrivastava, "Segmentation and Border Detection of Melanoma Lesions Using Convolutional Neural Network and SVM," in *Computational Intelligence: Theories, Applications and Future Directions-Volume I*, ed: Springer, 2019, pp. 97-108.
36. Nida, N., Irtaza, A., Javed, A., Yousaf, M. H., and Mahmood, M. T., Melanoma lesion detection and segmentation using deep region based convolutional neural network and fuzzy C-means clustering. Int. J. Med. Inform., 2019.
37. Nasir, M., Attique Khan, M., Sharif, M., Lali, I. U., Saba, T., and Iqbal, T., An improved strategy for skin lesion detection and classification using uniform segmentation and feature selection based approach. Microsc. Res. Tech. 81:528–543, 2018.
38. J. P. Ebenezer and J. C. Rajapakse, "Automatic segmentation of skin lesions using deep learning," *arXiv preprint arXiv: 1807.04893,* 2018.
39. Chambolle, A., An algorithm for total variation minimization and applications. J. Math. Imaging Vis. 20:89–97, 2004.
40. Rajchl, M., Yuan, J., White, J. A., Ukwatta, E., Stirrat, J., Nambakhsh, C. M. et al., Interactive hierarchical-flow segmentation of scar tissue from late-enhancement cardiac MR images. IEEE Trans. Med. Imaging 33:159–172, 2014.
41. Rousseau, F., Habas, P. A., and Studholme, C., A supervised patch-based approach for human brain labeling. IEEE Trans. Med. Imaging 30:1852–1862, 2011.
42. Zhuo, S., and Sim, T., Defocus map estimation from a single image. Pattern Recogn. 44:1852–1858, 2011.
43. A. Levin, D. Lischinski, Y. Weiss, "A closed form solution to natural image matting," in *Computer Vision and Pattern Recognition, 2006 IEEE Computer Society Conference on*, 2006, pp. 61-68.
44. P. Risholm, E. Samset, and W. Wells, "Bayesian estimation of deformation and elastic parameters in non-rigid registration," in *International Workshop on Biomedical Image Registration*, 2010, pp. 104-115.
45. P. Risholm, S. Pieper, E. Samset, and W. M. Wells, "Summarizing and visualizing uncertainty in non-rigid registration," in *International Conference on Medical Image Computing and Computer-Assisted Intervention*, 2010, pp. 554-561.
46. Simpson, I. J., Schnabel, J. A., Groves, A. R., Andersson, J. L., and Woolrich, M. W., Probabilistic inference of regularisation in non-rigid registration. NeuroImage 59:2438–2451, 2012.
47. Simpson, I. J., Woolrich, M. W., Andersson, J. R., Groves, A. R., and Schnabel, J., Ensemble learning incorporating uncertain registration. IEEE Trans. Med. Imaging 32:748–756, 2013.
48. W. Bai, W. Shi, D. P. O'Regan, T. Tong, H. Wang, S. Jamil-Copley, *et al.*, "A probabilistic patch-based label fusion model for multi-atlas segmentation with registration refinement: Application to cardiac MR images," IEEE Trans. Med. Imaging, vol. 32, pp. 1302-1315, 2013.
49. Coupé, P., Manjón, J. V., Fonov, V., Pruessner, J., Robles, M., and Collins, D. L., Patch-based segmentation using expert priors: Application to hippocampus and ventricle segmentation. NeuroImage 54:940–954, 2011.
50. Senthilselvi, A., and Sukumar, R., Removal of salt and pepper noise from images using hybrid filter (HF) and fuzzy logic noise detector (FLND). J. Concur. Comput. Pract. Exp., 2018. https://doi.org/10.1002/cpe.4501.
51. Senthilselvi, A., and Sukumar, R., A survey on image restoration technique. Int. J. Emerg. Eng. Res. Technol. 2(8):123–128, 2014.
52. Flusser, J., and Suk, T., Pattern recognition by affine moment invariants. Pattern Recogn. 26:167–174, 1993.
53. Hu, M.-K., Visual pattern recognition by moment invariants. IRE Trans. Inform. Theory 8:179–187, 1962.
54. Sadeghi, M., Razmara, M., Lee, T. K., and Atkins, M. S., A novel method for detection of pigment network in dermoscopic images using graphs. Comput. Med. Imaging Graph. 35:137–143, 2011.
55. C. Szegedy, V. Vanhoucke, S. Ioffe, J. Shlens, and Z. Wojna, "Rethinking the inception architecture for computer vision," in *Proceedings of the IEEE conference on computer vision and pattern recognition*, 2016, pp. 2818-2826.

56. Satheesha, T., Satyanarayana, D., Prasad, M. G., and Dhruve, K. D., Melanoma is skin deep: A 3D reconstruction technique for computerized dermoscopic skin lesion classification. IEEE J Trans. Eng. Health Med. 5:1–17, 2017.
57. T. Mendonça, P. M. Ferreira, J. S. Marques, A. R. Marcal, and J. Rozeira, "PH 2-A dermoscopic image database for research and benchmarking," in *Engineering in Medicine and Biology Society (EMBC), 2013 35th Annual International Conference of the IEEE*, 2013, pp. 5437-5440.
58. A. A. Marghoob, R. P. Braun, and A. W. Kopf, *Interactive CD-ROM of Dermoscopy*: Informa Healthcare, 2007.
59. G. Argenziano, H. Soyer, V. De Giorgi, D. Piccolo, P. Carli, and M. Delfino, "Interactive atlas of dermoscopy (Book and CD-ROM)," 2000.
60. H. Soyer, G. Argenziano, S. Chimenti, S. Menzies, H. Pehamberger, H. Rabinovitz, *et al.*, "Dermoscopy of pigmented skins lesions. An Atlas based on the Consensus Net Meeting on Dermoscopy 2000," 2001.